



Cite this: *J. Mater. Chem. C*, 2016, 4, 3125

Received 23rd February 2016,
Accepted 26th February 2016

DOI: 10.1039/c6tc00681g

www.rsc.org/MaterialsC

Back-contacted hybrid organic–inorganic perovskite solar cells†

A. N. Jumabekov,^{*a} E. Della Gaspera,^{‡a} Z.-Q. Xu,^b A. S. R. Chesman,^a
J. van Embden,^c S. A. Bonke,^d Q. Bao,^{eb} D. Vak^a and U. Bach^{*ab}

A novel architecture for quasi-interdigitated electrodes (QIDEs) allows for the fabrication of back-contacted perovskite solar cells. The devices showed a stable power output of 3.2%. The design of the QIDEs avoids the defects that cause short-circuiting in conventional IDEs, while enhancing the collection area of the electrodes. Photoluminescence and photocurrent mapping is used to probe the charge generation and transport properties of the perovskite solar cells.

Hybrid organic–inorganic perovskites have been identified as one of the most promising class of materials for photovoltaic and optoelectronic applications, due to their excellent electronic and optical properties, combined with their ease of fabrication.^{1–3} In the past few years, these materials have garnered significant attention in the photovoltaic community, despite their moisture and oxygen instability and the requirement of harmful precursor materials. The development of the power conversion efficiency (PCE) of solid-state devices incorporating perovskite absorber layers has progressed at an incredibly rapid pace, with the current certified PCE of a champion solar cell (SC) device with a formamidinium lead iodide perovskite absorber layer at 20.1%.⁴

Conventional solid-state hybrid organic–inorganic perovskite-based solar cells have a sandwich type structure, as shown in Fig. 1a. The perovskite absorber layer is positioned between top and bottom electrodes, typically a transparent conducting oxide (TCO) layer on a glass and an evaporated thin layer of gold or silver, respectively. Furthermore, perovskite SCs typically

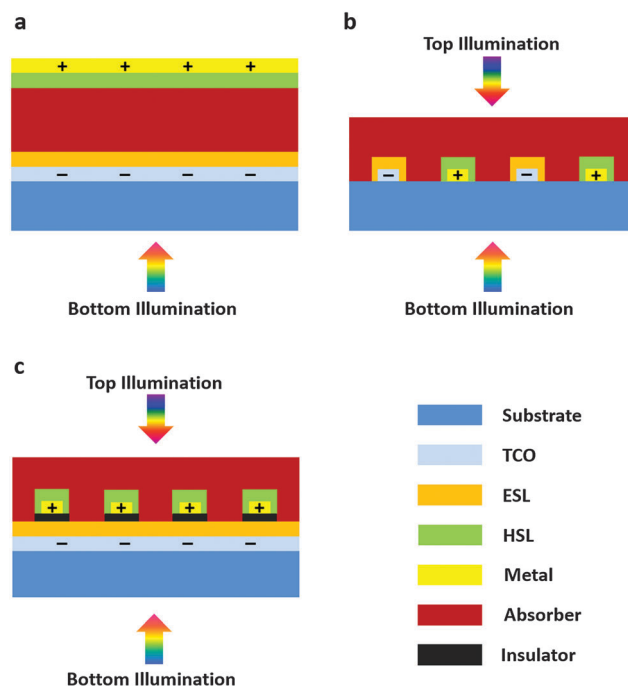


Fig. 1 Comparison of SCs with different architectures; (a) standard sandwich type, (b) IDE-based back-contacted type and (c) novel QIDE-based back-contacted type.

comprise an additional electron selective layer (ESL), such as TiO_2 , ZnO or PCBM, and spiro-OMeTAD, NiO or CuSCN acting as a hole selective layer (HSL) between the perovskite absorber layer and each electrode.^{2–6} However, devices with only one charge selective layer can also generate a stable power output under illumination.^{7,8} In the conventional device architecture, illumination of the cells is performed from the TCO side (bottom illumination).

An alternative, more sophisticated, architecture for SC devices, which is utilized in Si-based and dye-sensitized SCs, incorporates a back-contact electrode.^{9,10} In this configuration both electrodes of the cell are positioned on only one side of the absorber layer,

^a CSIRO Manufacturing, Clayton, Victoria 3168, Australia.

E-mail: askhat.jumabekov@csiro.au

^b Department of Materials Science & Engineering, Monash University, Clayton, Victoria 3800, Australia. E-mail: udo.bach@monash.edu

^c School of Science, RMIT University, Melbourne, Victoria 3001, Australia

^d School of Chemistry, Monash University, Clayton, Victoria 3800, Australia

^e Institute of Functional Nano and Soft Materials (FUNSOM), Jiangsu Key Laboratory for Carbon-Based Functional Materials and Devices, and Collaborative Innovation Center of Suzhou Nano Science and Technology, Soochow University, Suzhou 215123, China

† Electronic supplementary information (ESI) available. See DOI: 10.1039/c6tc00681g

‡ Current address: School of Science, RMIT University, Melbourne, Victoria 3001, Australia.

with the electrodes and the respective charge transporting layers typically arranged in an interdigitated fashion (Fig. 1b). The solar cell is completed by depositing the absorber layer on top of the interdigitated electrode (IDE). In the case of this architecture illumination of the device occurs typically from the absorber layer side (top illumination). However, illumination through the bottom is also possible when a TCO coated glass is employed as the substrate. Remarkable PCEs of above 22% were achieved with back-contacted Si-based solar cells using IDEs.¹¹ The main advantage of the back-contacted architecture over the sandwich structure employed in conventional SCs is that illumination from the photoactive layer side avoids the occurrence of transmission losses caused by the charge collecting top electrode.

The charge diffusion length within a perovskite layer made using standard fabrication methods is usually within the range of a few microns.^{12–14} Therefore, the spacing between the fingers of the IDE needs to be in the same range or smaller in order to achieve efficient charge extraction, which is a requirement in all high efficiency back-contacted SC devices. The fabrication of IDEs usually involves photolithographic techniques, which, according to our experience, are prone to forming defects and short-circuit pathways in the IDE architecture (see Fig. S1, ESI†). In light of this, we have developed an alternative IDE configuration, following a more defect-tolerant design. One way to create a more robust architecture is to deposit only one set of electrode fingers or a grid on top of an unpatterned charge collection electrode, separated by a charge selective layer and an insulating layer, as shown in Fig. 1c. As these fingers resemble a traditional IDE architecture this design may be referred to as a quasi-interdigitated electrode (QIDE). QIDEs can also be fabricated using the same techniques as those used for IDEs; however, the advantage of QIDEs is that the physical gap between collecting fingers also work as a finger, so there is no electro-inactive area. This practically doubles the maximum finger density for a given processing resolution compared to a traditional IDE structure. Therefore, the distance between electrodes in a lateral direction is significantly reduced in QIDE.

Recently, Xiao *et al.* reported a device that consists of a perovskite layer deposited on a bare gold IDE on a glass substrate, with 8 μm electrode spacing and no ESL or HSL present over the gold fingers.¹⁵ The authors demonstrated that the device shows an impermanent photovoltaic effect under illumination after applying 10 V (poling) for 100 s across the gold IDEs. However, no photovoltaic effect is observed without poling and poling is also not sufficient to provide a significant stabilized power output when these cells are operated at their maximum power point. In this work, we use QIDEs (see Fig. 1c) for the fabrication of the first back-contacted solid-state perovskite solar cell with charge selective electrodes. We use photolithographic and vacuum-based deposition techniques for the fabrication of the QIDEs on an indium tin oxide (ITO) glass substrate with all-inorganic electron and hole selective layers. A gas-assisted deposition method is used to grow a methylammonium lead iodide perovskite absorber layer on top of the electrodes to complete the device fabrication.¹⁶ The maximum PCE achieved with our novel cell architecture under standard AM 1.5 at 1 Sun illumination is over 6.0%. The devices showed a stable photovoltaic performance when monitored at the maximum power point (MPP).

We started the QIDE fabrication by sputtering a ~ 50 nm ZnO layer onto a patterned ITO glass substrate (Fig. 2a(i) and Fig. S2, ESI†). A polymer mask with the desired features was

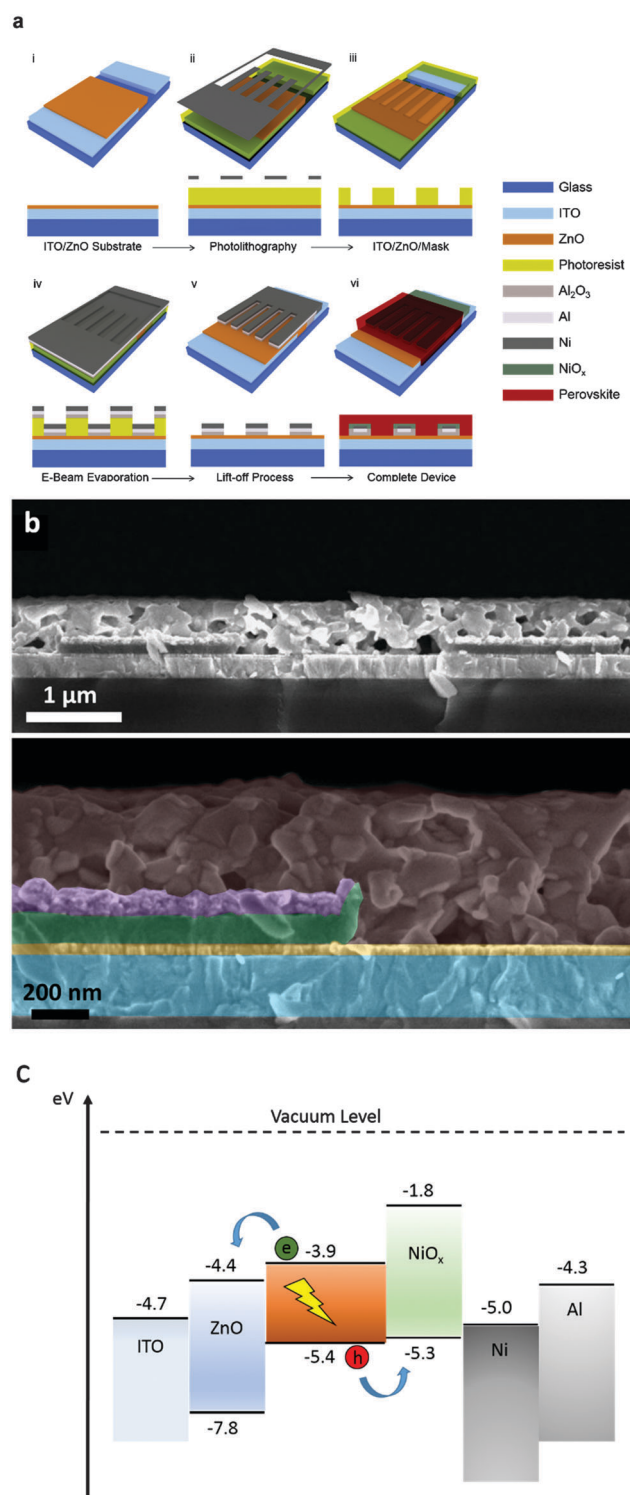


Fig. 2 (a) Schematic representation of the QIDE and back-contacted SC device fabrication processes. (b) Cross-sectional SEM image of a back-contacted perovskite SC device. Top image at 15 000 \times magnification, the bottom image at 45 500 \times magnification. (c) Approximate band diagram of the back-contacted perovskite SC.

then deposited *via* a photolithographic technique. For this, a $\sim 2\ \mu\text{m}$ thick photoresist layer was spin coated onto the substrate and exposed to UV light through a chrome photo-mask with the desired pattern, as shown in the perspective (3D) and cross-sectional views in Fig. 2a(ii). The UV-exposed parts of the photoresist layer were removed in the developmental step by washing the substrate in a developer solution, thus leaving a portion of the substrate protected by the photoresist mask (Fig. 2a(iii)). In the next step, 100 nm Al_2O_3 , 30 nm Al and 50 nm Ni layers were sequentially evaporated onto the substrate using an electron-beam evaporator (Fig. 2a(iv)). Then, the remainder of the polymer mask was removed by washing the substrates in acetone (lift-off process), leaving fingers of the evaporated materials (Fig. 2a(v) and Fig. S3, ESI†). The QIDE was completed by heat-treating the electrodes at $300\ ^\circ\text{C}$, which created an oxide layer shell (Al_2O_3 and NiO_x) around the metallic parts of the electrodes. The formation of a NiO or NiO_x layer during the heat treatment process was verified indirectly by photoelectron spectroscopy in air (PESA) measurements (Fig. S4, ESI†), indicating a $+0.5\ \text{eV}$ work function shift.¹⁷ In the complete QIDE, the two charge collecting electrodes (ITO and Al/Ni) are continuously covered and separated by oxide layers, in which the ZnO layer acts as the ESL and the NiO_x as the HSL (Fig. 2a(vi) and Fig. S2, ESI†). Finally, to complete the device fabrication, a perovskite precursor solution was deposited onto the QIDE using a gas-assisted spin coating method, followed by annealing at $100\ ^\circ\text{C}$ to form a thin, crystalline $\text{CH}_3\text{NH}_3\text{PbI}_3$ perovskite absorber layer on top of the QIDEs (Fig. S2, ESI†).

The cross-sectional micrograph of the complete device, obtained by scanning electron microscopy (SEM), is shown in Fig. 2b. The SEM image at lower magnification (see the top image in Fig. 2b) shows the $2\ \mu\text{m}$ wide and $\sim 200\ \text{nm}$ thick fingers of the QIDE separated by a $2\ \mu\text{m}$ gap on the glass/ITO/ ZnO substrate, and a $\sim 500\ \text{nm}$ thick $\text{CH}_3\text{NH}_3\text{PbI}_3$ perovskite absorber layer on top. The bottom image in Fig. 2b shows a magnified cross-sectional image of the device with each layer color-coded for easy identification. The absorber layer covers the QIDE homogeneously, with the apparent crystallite size of $\text{CH}_3\text{NH}_3\text{PbI}_3$ varying from tens to hundreds of nanometers. Fig. 2c shows an approximate band alignment diagram and a mechanism for the charge generation and separation processes in the device. In the band diagram the Al_2O_3 layer is omitted as it only acts as a spacer between the anode and the cathode and has no role in charge generation and separation processes.

Once the QIDE deposition process was optimized, the fabrication of a batch of 20 QIDE substrates was highly unlikely to yield a single defective substrate that suffered from obvious short-circuits between the two charge collecting electrodes. The high defect tolerance of this fabrication process arises from the fact that the same photoresist mask is used during the sequential deposition of Al_2O_3 , Al and Ni. Fig. 2b provides further evidence that the initial Al_2O_3 deposition process produces a trough-like insulator structure, indicating that some Al_2O_3 coverage of the photoresist walls has occurred during the fabrication process. This further ensures that a direct electrical contact between the two charge collecting electrodes can successfully be avoided.

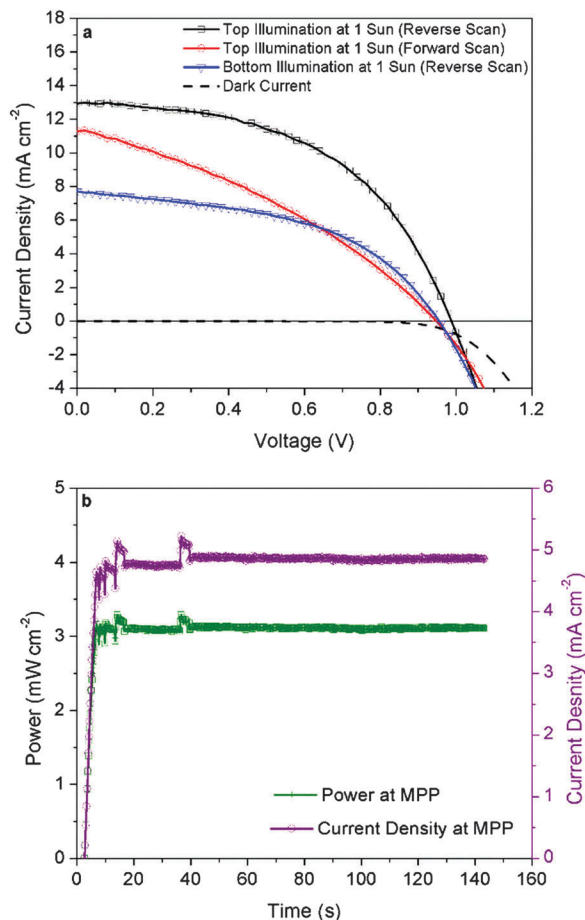


Fig. 3 (a) J - V characteristics of the back-contacted perovskite SC device. (b) Time dependent measurements of the photocurrent and power densities at the maximum power point.

Fig. 3a shows the J - V characteristics of the back-contacted SC device. In reverse scan mode ($V_{\text{OC}} \rightarrow 0$), the J - V curve for top illumination at 1 Sun shows values of $12.95\ \text{mA cm}^{-2}$, $0.98\ \text{V}$ and 51.5% for the short-circuit current density (J_{SC}), open-circuit voltage (V_{OC}) and fill factor, respectively. On the other hand, in forward scan mode ($0 \rightarrow V_{\text{OC}}$), J_{SC} , V_{OC} and fill factor values are $11.28\ \text{mA cm}^{-2}$, $0.94\ \text{V}$ and 34.7% , respectively. The PCE of the device in reverse scan mode is 6.54% , whereas in forward scan mode it is 3.68% . Such a significant dissimilarity between the J - V characteristics in the reverse and forward scan modes is the result of the so-called hysteresis phenomenon, which has been reported repeatedly for perovskite devices with a conventional electrode architecture.^{18–20}

Bottom illumination of the cells under 1 Sun condition shows values of $7.7\ \text{mA cm}^{-2}$, $0.95\ \text{V}$ and 48.11% for J_{SC} , V_{OC} and fill factor, respectively, thus resulting in a PCE value of 3.52% . This is in accordance with light transmission measurements (see Fig. S5 in the ESI†) on the QIDE, which showed that the metallic fingers of the electrode reflect approximately half of the light when illuminated from the bottom compared to a blank ITO glass substrate. Fig. 3b shows the result of monitoring the current density and power at the maximum power point (MPP) under 1 Sun condition (top illumination) as a function of

time. Overall, the device shows a stable power output with a value of around 3.2% maintained throughout the measurements. Comparison of the PCEs obtained from the J - V and MPP tracking measurements shows that the stabilized PCE of the device is close to the value obtained from the forward scan.

To understand the operating principles of the back-contacted perovskite SC device, spatial photoluminescence (PL) and photocurrent (PC) mapping were performed in top and bottom illumination modes.²¹ The size of the investigated area was $21 \times 21 \mu\text{m}^2$ and encloses the 'bay' as well as a portion of the 'quasi-interdigitated' region (see Fig. 4m and Fig. S6, ESI†). The 'bay' refers to an unpatterned area of Al/Ni/NiO_x covered with perovskite. Fig. 4a–f show the PL and PC intensity maps for the top illumination mode. Likewise, Fig. 4g–l show the PL and PC intensity maps for the bottom illumination

mode. For both sets of measurements the device was monitored using moderate forward (0.2 V), short-circuit (0 V) and reverse (−0.2 V) bias potentials. In Fig. 4a–c (top illumination) the lower PL intensity regions (dark parts) correspond to the perovskite layer over the ZnO, while the higher PL intensity regions (bay and fingers) are over the NiO_x. Alternatively, in the bottom illumination case, the PL intensity from the perovskite now located under the NiO_x is lower than that under ZnO. This is due to the metal layers lying over the NiO_x blocking the PL signal. Generally, the photoluminescence map has a very patchy appearance, an observation that is in agreement with earlier observations by Ginger and co-workers.²² A comparison of the PL mapping (Fig. 4a–c) with the PC mapping (Fig. 4d–f) in the top illumination mode suggests that charge collection over ZnO is more efficient than over NiO_x. This could be due to

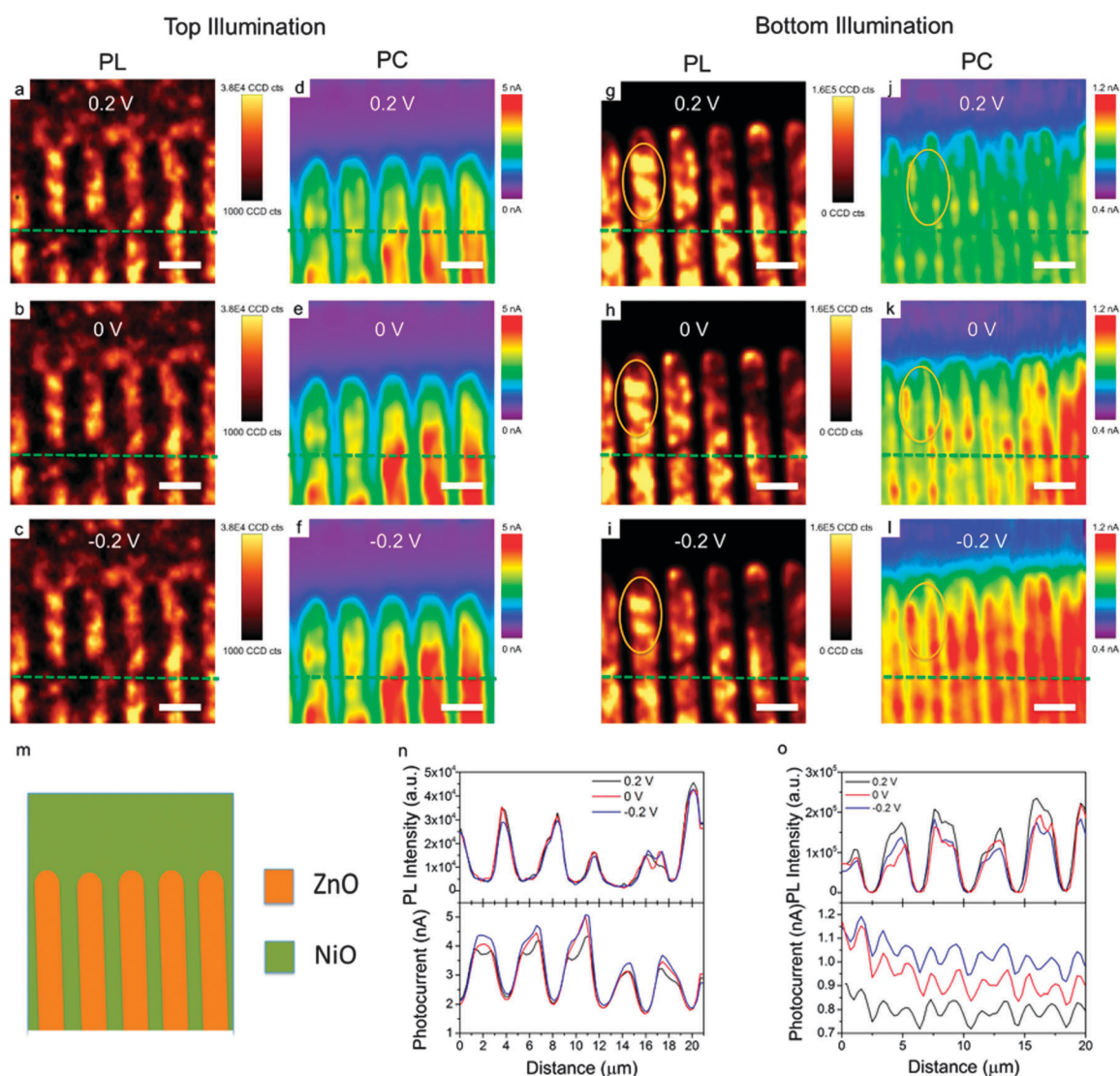


Fig. 4 (a–c) PL intensity maps (integrated from 700 nm to 778 nm) and (d–f) spatial PC maps with laser illumination from the top (absorber side) of the device operating under a bias of (a) and (d) 0.2 V, (b) and (e) 0 V, (c) and (f) −0.2 V, respectively. Scale bar: 4 μm . (g–i) PL intensity maps (integrated from 700 nm to 778 nm) and (j–l) spatial photocurrent maps with laser illumination from the bottom (TCO side) of the device operating under a bias of (g) and (j) 0.2 V, (h) and (k) 0 V, (i) and (l) −0.2 V, respectively. Scale bar: 4 μm . (m) Schematic layout of the electrode in the analysis of PL and PC maps. (n) PL intensity and PC profiles along the green dashed lines in (a–c) and (d–f). (o) The PL intensity and PC profiles along the green dashed lines in (g–i) and (j–l).

the lower driving force for interfacial charge transfer at the NiO_x /perovskite interface arising from the lower band offset compared to ZnO /perovskite (see Fig. 2c). In both illumination modes (bottom and top) the photocurrent densities are inhomogeneous over the scanned area and significantly lower both in the center of the NiO_x finger, as well as in the center of the finger-gap (center of a ZnO collection electrode). The 'hot spot' for charge collection seems to be near the edge of the finger electrodes, where the hole- and electron collecting electrodes are only separated by a 100 nm thick Al_2O_3 layer. This is evidenced by the appearance of double peaks when the PL and PC profiles along the same cross-section (green dashed lines) are plotted together (see Fig. 4n and o). As expected, PC mapping in both illumination modes shows no photocurrent over the bay area.

The PL and PC intensity maps in the top illumination mode show only a very minor potential dependence. This is in stark contrast to the much more pronounced potential dependence observed in the bottom illumination mode. Generally, in both illumination modes the PL maps show an overall decrease in photoluminescence intensity (see parts indicated with oval circle in Fig. 4g–i) and the PC maps show an overall increase in photocurrent intensity when moving from forward to reverse bias conditions (see parts indicated with oval circles in Fig. 4j–l). The different bias dependences of the PC and PL intensities between top and bottom illumination modes can be rationalized by the presence of a localized electric field near the edge of the finger electrodes. The applied bias changes will significantly change the magnitude of the local electric field within the perovskite layer close to this junction, resulting in a significantly larger bias dependence in the bottom illumination, compared to the top illumination mode. Furthermore, we expect that the maximized local electric field close to the QIDE surface (at the boundary of the anode and cathode) will decay quickly when moving away from the QIDE surface due to the high dielectric constant, ϵ_r , of the perovskite (~ 70).^{23–26} In addition, the perovskite layer has a very high extinction coefficient at the laser wavelength (532 nm) used for photocurrent mapping. As a result, the majority of the charge carriers are generated in close vicinity to either the perovskite/air or perovskite/QIDE interface when illuminated from the top or bottom, respectively. Therefore, in bottom illumination mode the charge carriers can be more effectively picked up by the electric field generated by the small applied bias, compared to top illumination mode.

Conclusions

In conclusion, we have shown a fabrication process for back-contacted perovskite SCs using a simple and novel architecture. We demonstrated that the device produces a stable power output and can be illuminated from either the absorber or glass substrate side. Characterization of the devices with PL and PC mapping techniques showed that the photocurrent collection is inhomogeneous throughout the active area of the cell and is most efficient near the interface between the ESL and the HSL. This suggests that a smaller gap between the fingers of

the QIDE could potentially improve charge collection, resulting in more homogenous and higher photocurrent collection efficiency. Additionally, it is expected that a better cell performance, as well as reduced J - V hysteresis, can be achieved by the fabrication of a perovskite layer with larger grains and better crystallinity, which will lead to a longer diffusion length.^{27,28} The PL and PC mapping experiments indicate less efficient charge collection from the HSL than the ESL. We concluded that an improved performance could be achieved by the careful selection of a HSL material that can give a better band offset with the perovskite for a higher driving force for hole extraction.

The high intrinsic defect tolerance of the QIDE structure and the effective doubling of the process resolution potentially make the electrode amenable to printing, allowing for it to be applied to the future large scale production of perovskite SCs. Although photolithography was used to demonstrate the proof of concept for this architecture, we believe this structure can also be fabricated by cheap alternative methods such as reverse-offset printing, which can produce sub-micron patterns.²⁹ Once the processes and materials are further developed, the innovative device configuration will be a very attractive alternative to the conventional sandwich structure currently employed in a range of applications in the field of photovoltaic and other optoelectronic devices. The back-contact devices will also be useful for conducting fundamental studies as it has an exposed photoactive area, permitting *in situ* measurements on the effects of chemical treatment or passivation.

Acknowledgements

This work was performed in part at the Melbourne Centre for Nanofabrication (MCN) in the Victorian Node of the Australian National Fabrication Facility (ANFF). The authors thank Dr Ricky T. Tjeung and Dr Yang Choon Lim from the MCN for their valuable advice and assistance with the photolithography and electron-beam evaporation techniques. The authors are also thankful to Dr Alexander R. Pascoe from Monash University for sharing his ideas on perovskite crystal growth mechanisms, and Dr Kallista Sears for her help with the PESA measurements. This work was funded through CSIRO Manufacturing as part of an Office of the Chief Executive Postdoctoral Fellowship (A. N. J.) and Science Leader Fellowship (U. B.). A. S. R. C. acknowledges the Australian Research Council for funding through a DECRA Fellowship. Q. B. acknowledges support from the National Natural Science Foundation of China (Grant No. 91433107), the Youth 973 Program (Grant No. 2015CB932700), ARC DECRA (DE120101569) and DP (DP140101501). The authors also acknowledge the financial support from the Australian Renewable Energy Agency (ARENA) and the Australian Centre for Advanced Photovoltaics (ACAP).

Notes and references

- 1 A. Kojima, K. Teshima, Y. Shirai and T. Miyasaka, *J. Am. Chem. Soc.*, 2009, **131**, 6050.
- 2 H.-S. Kim, C.-R. Lee, J.-H. Im, K.-B. Lee, T. Moehl, A. Marchioro, S.-J. Moon, R. Humphry-Baker, J.-H. Yum,

- J. E. Moser, M. Grätzel and N.-G. Park, *Sci. Rep.*, 2012, 2(591), 1.
- 3 M. M. Lee, J. Teuscher, T. Miyasaka, T. N. Murakami and H. J. Snaith, *Science*, 2012, **338**, 643.
- 4 W. S. Yang, J. H. Noh, N. J. Jeon, Y. C. Kim, S. Ryu, J. Seo and S. I. Seok, *Science*, 2015, **348**, 1234.
- 5 M. A. Green, A. Ho-Baillie and H. J. Snaith, *Nat. Photonics*, 2014, **8**, 506.
- 6 M. Liu, M. B. Johnston and H. J. Snaith, *Nature*, 2013, **501**, 395.
- 7 A. R. Pascoe, N. W. Duffy, A. D. Scully, F. Huang and Y.-B. Cheng, *J. Phys. Chem. C*, 2015, **119**, 4444.
- 8 A. Mei, X. Li, L. Liu, Z. Ku, T. Liu, Y. Rong, M. Xu, M. Hu, J. Chen, Y. Yang, M. Grätzel and H. Han, *Science*, 2014, **345**, 295.
- 9 P. J. Verlinden, R. M. Swanson and R. A. Crane, *Prog. Photovoltaics*, 1994, **2**, 143.
- 10 D. Fu, X. L. Zhang, R. L. Barber and U. Bach, *Adv. Mater.*, 2010, **22**, 4270.
- 11 H. Savin, P. Repo, G. von Gastrow, P. Ortega, E. Calle, M. Garín and R. Alcubilla, *Nat. Nanotechnol.*, 2015, **10**, 624.
- 12 S. D. Stranks, G. E. Eperon, G. Grancini, C. Menelaou, M. J. P. Alcocer, T. Leijtens, L. M. Herz, A. Petrozza and H. J. Snaith, *Science*, 2013, **342**, 341.
- 13 D. Shi, V. Adinolfi, R. Comin, M. Yuan, E. Alarousu, A. Buin, Y. Chen, S. Hoogland, A. Rothenberger, K. Katsiev, Y. Losovyj, X. Zhang, P. A. Dowben, O. F. Mohammed, E. H. Sargent and O. M. Bakr, *Science*, 2015, **347**, 519.
- 14 Q. Dong, Y. Fang, Y. Shao, P. Mulligan, J. Qiu, L. Cao and J. Huang, *Science*, 2015, **347**, 967.
- 15 Z. Xiao, Y. Yuan, Y. Shao, Q. Wang, Q. Dong, C. Bi, P. Sharma, A. Gruverman and J. Huang, *Nat. Mater.*, 2015, **14**, 193.
- 16 F. Huang, Y. Dkhissi, W. Huang, M. Xiao, I. Benesperi, S. Rubanov, Y. Zhu, X. Lin, L. Jiang, Y. Zhou, A. Gray-Weale, J. Etheridge, C. R. McNeill, R. A. Caruso, U. Bach, L. Spiccia and Y.-B. Cheng, *Nano Energy*, 2014, **10**, 10.
- 17 J. Jasieniak, M. Califano and S. E. Watkins, *ACS Nano*, 2011, **5**, 5888.
- 18 H. J. Snaith, A. Abate, J. M. Ball, G. E. Eperon, T. Leijtens, N. K. Noel, S. D. Stranks, J. T.-W. Wang, K. Wojciechowski and W. Zhang, *J. Phys. Chem. Lett.*, 2014, **5**, 1511.
- 19 E. L. Unger, E. T. Hoke, C. D. Bailie, W. H. Nguyen, A. R. Bowring, T. Heumüller, M. G. Christoforo and M. D. McGehee, *Energy Environ. Sci.*, 2014, **7**, 3690.
- 20 W. Tress, N. Marinova, T. Moehl, S. M. Zakeeruddin, M. K. Nazeeruddin and M. Grätzel, *Energy Environ. Sci.*, 2015, **8**, 995.
- 21 H. Qiao, J. Yuan, Z. Xu, C. Chen, S. Lin, Y. Wang, J. Song, Y. Liu, Q. Khan, H. Y. Hoh, C.-X. Pan, S. Li and Q. Bao, *ACS Nano*, 2015, **9**, 1886.
- 22 D. W. deQuilettes, S. M. Vorpahl, S. D. Stranks, H. Nagaoka, G. E. Eperon, M. E. Ziffer, H. J. Snaith and D. S. Ginger, *Science*, 2015, **348**, 683.
- 23 E. J. Juarez-Perez, R. S. Sanchez, L. Badia, G. Garcia-Belmonte, Y. S. Kang, I. Mora-Sero and J. Bisquert, *J. Phys. Chem. Lett.*, 2014, **5**, 2390.
- 24 A. Pockett, G. E. Eperon, T. Peltola, H. J. Snaith, A. Walker, L. M. Peter and P. J. Cameron, *J. Phys. Chem. C*, 2015, **119**, 3456.
- 25 Q. Lin, A. Armin, R. C. R. Nagiri, P. L. Burn and P. Meredith, *Nat. Photonics*, 2015, **9**, 106.
- 26 D. P. Almond and C. R. Bowen, *J. Phys. Chem. Lett.*, 2015, **6**, 1736.
- 27 W. Nie, H. Tsai, R. Asadpour, J.-C. Blancon, A. J. Neukirch, G. Gupta, J. J. Crochet, M. Chhowalla, S. Tretiak, M. A. Alam, H.-L. Wang and A. D. Mohite, *Science*, 2015, **347**, 522.
- 28 J. K. Park, J. H. Heo, H. J. Han, M. H. Lee, D. H. Song, M. S. You, S.-J. Sung, D.-H. Kim and S. H. Im, *Nanotechnology*, 2016, **27**, 024004.
- 29 K. Fukuda, Y. Yoshimura, T. Okamoto, Y. Takeda, D. Kumaki, Y. Katayama and S. Tokito, *Adv. Electron. Mater.*, 2015, **1**, 1500145.